ORIGINAL RESEARCH **Open access**

UAV Magnetometry for Geological Mapping and Material Characterization in Mining Areas

Youssef Hariri[1*], Hassan Nasser[1], Fatima Zahra[2]

Abstract

The geological framework and material distribution within the Lavrion repository in Greece are examined through an airborne magnetometry campaign that employs an original unmanned aerial platform, CERBERUS, and sophisticated data-handling workflows. Utilizing UAV-based magnetometry provided a detailed, non-destructive means of recording magnetic field measurements over complex, potentially hazardous ground (heavily contaminated soils), enabling rapid, precise mapping of the surveyed area. The final deliverable consisted of a 3D magnetic susceptibility volume depicting a granular representation of susceptibility shifts within the repository. This volumetric construction enabled a clear visual interpretation of elevated-susceptibility sectors associated with ferromagnetic constituents and reduced-susceptibility sectors linked to diamagnetic substances, including lead, arsenic, cadmium, and zinc. The integrated methods emphasize the effectiveness of UAV-deployed aerial magnetometry in geophysical investigations, highlighting its applicability to mineral prospecting and waste management. The research confirms that integrating unmanned aircraft platforms with magnetic information analysis yields a robust instrument for securely, productively, and nonintrusively investigating subterranean configurations.

Keywords Mining, Exploration, Waste management, Drone, Magnetometer, 3D inversion models

*Correspondence:
Youssef Hariri
youssef.hariri@um5.ac.ma
[1] Department of AI for Argan Tree and Cereal Crop Monitoring, Faculty of Agriculture, Mohammed V University, Rabat, Morocco
[2] Department of Soil Nutrient Prediction using Remote Sensing, Faculty of Agriculture, University of Casablanca, Casablanca, Morocco

Introduction

Mineral extraction operations are scaling up at a remarkable pace, driven by escalating demand for minerals, particularly metals that support the current shift toward sustainable energy. Over the past few decades, the field has grappled with a series of challenges aimed at boosting output while meeting current requirements. As ore concentrations decline, the prevalence of deeper-seated deposits and more resistant rock masses, combined with heightened societal and ecological consciousness, has compelled mineral extraction endeavors to continually adapt to these emerging circumstances [1, 2].

Notwithstanding the evident and intensifying need for resource discovery and extraction, numerous players in the extraction sector argue that the industry remains at an early stage of the overhaul driven by global digital evolution. However, the alterations and novel approaches embedded across every segment of a mining workflow are considerable, signifying that technical breakthroughs are and will continue to be pivotal to the prospective advancement of the mining domain [3, 4].

This is an open access article distributed under the terms of the Creative Commons Attribution-NonCommercial-ShareAlike 4.0 International License (CC BY-NC-SA 4.0), which permits non-commercial use, distribution, reproduction, and adaptation in any medium or format, provided that appropriate credit is given to the original author(s) and source, a link to the license is provided, and any changes made are indicated. Adapted material must be distributed under the same license.

© 2022 The Author(s). | Published by Agro Intelligence Research Press

In relation to one of the most vital steps of the mining cycle, prospecting is viewed as an elaborate undertaking that requires formulating a data-acquisition and conceptual-modeling scheme capable of distinctly outlining zones of promise within a particular ore body. Within this framework, the recent arrival of compact Unmanned Aerial Vehicles (UAVs) equipped with diverse sensing instruments has established a formidable resource for geospatial mapping and reconnaissance [5, 6]. Even though the predominant drones are used for capturing and manipulating aerial imagery, downsizing geophysical instrumentation has unlocked new avenues for integrating airborne sensors. Illustrations of such progress in subsurface surveying include the deployment of UAV-transported ground-penetrating radar systems [7, 8], copter-mounted magnetometer rigs [9-12], and drones outfitted with Light Detection and Ranging (LiDAR) systems for bathymetric surveying [13]. These synergies prove especially crucial when the scale of the terrain to be investigated is overly expansive or ground-based access is unfeasible for executing standard survey protocols.

Centering on geomagnetic techniques, considered among the most powerful means for resource scouting, these assessments have habitually been conducted at ground level, shifting the sensing apparatus by hand and obtaining finely resolved spatial measurements at the expense of operational speed [14-17]. The reality is that, although the geomagnetic field intelligence arrives with very fine spatial granularity, the equipment must be conveyed along every transect, an arduous operation over rough landforms like outcrops or marshlands [18]. For this reason, integrating copter platforms into this sphere delivers manifold benefits, such as reduced logistical burdens, greater adaptability, and simpler operations. Indeed, UAV-mounted magnetometers allow blending the speed and coverage typical of copter surveys with the granularity of standard walk-over systems [19].

Acknowledging the criticality of broadening the adoption of these state-of-the-art airborne exploration frameworks within the extractive sectors, the present work focuses on evaluating the capability of operating a copter-slung magnetometer for the investigation of a defined legacy mining zone. To achieve this, a pioneering UAV apparatus has been fashioned to carry a magnetic sensing payload, accounting for potential functional constraints, such as the instrument's dimensions and heft, the clearance between the copter and the magnetic pickup, and assorted variables tied to aerial maneuver conditions. In addition to this fresh technical advancement, the investigation unfolds in a meaningful mining scenario where the precise identification of valuable elements serves as a linchpin for restoring former mining sites and achieving efficient metallic reclamation. On this premise, the document unfolds as follows. Firstly, a portrayal of the site's geological backdrop and overall setting is tendered in Section 2. Section 3 presents a methodological portion outlining the merged sensor-UAV ensemble utilized for the prospecting flyovers, along with the data capture and refinement sequence. The primary outcomes emerging from the geophysical data gathering are delineated in Section 4. A concluding segment is assigned to emphasize the main discoveries drawn from deploying the technique within the distinctive mining environment.

Geological Context of the Lavrion District

Lavrion rests at the extreme southern end of the Attica Peninsula in southern Greece, about 60 km southeast of the nation's capital, Athens. It ranks among the globe's most ancient extractive zones, with operational records extending back to the second millennium BC. Extractive and pyrometallurgical activities persisted, even amid numerous hiatuses, until the termination of World War II, eventually halting completely by the 1970s [20].

The Lavrion terrain, belonging to the Attic–Cycladic crystalline mass, is constructed from three principal Alpine-orogeny tectonic nappes **(Figure 1a)**: the Kamariza slice (or Lower structural stack), the Lavrion blueschist slice (or Middle structural stack), and the Berzekos slice (or Upper structural stack) [21]. The foundational Kamariza slice incorporates two marble strata spanning the Late Triassic to Early Jurassic, designated the Upper and Lower marble, alongside the unit termed Kamariza schists. The Lavrion slice, spanning the Late Jurassic to Cretaceous, lies structurally above the Kamariza slice and comprises Lavrion schist, marbles, and a meta-ophiolitic complex. The Upper Cycladic slice appears only sporadically and is formed of Upper Cretaceous micritic limestone [22].

© 2022 The Author(s). | Published by Agro Intelligence Research Press

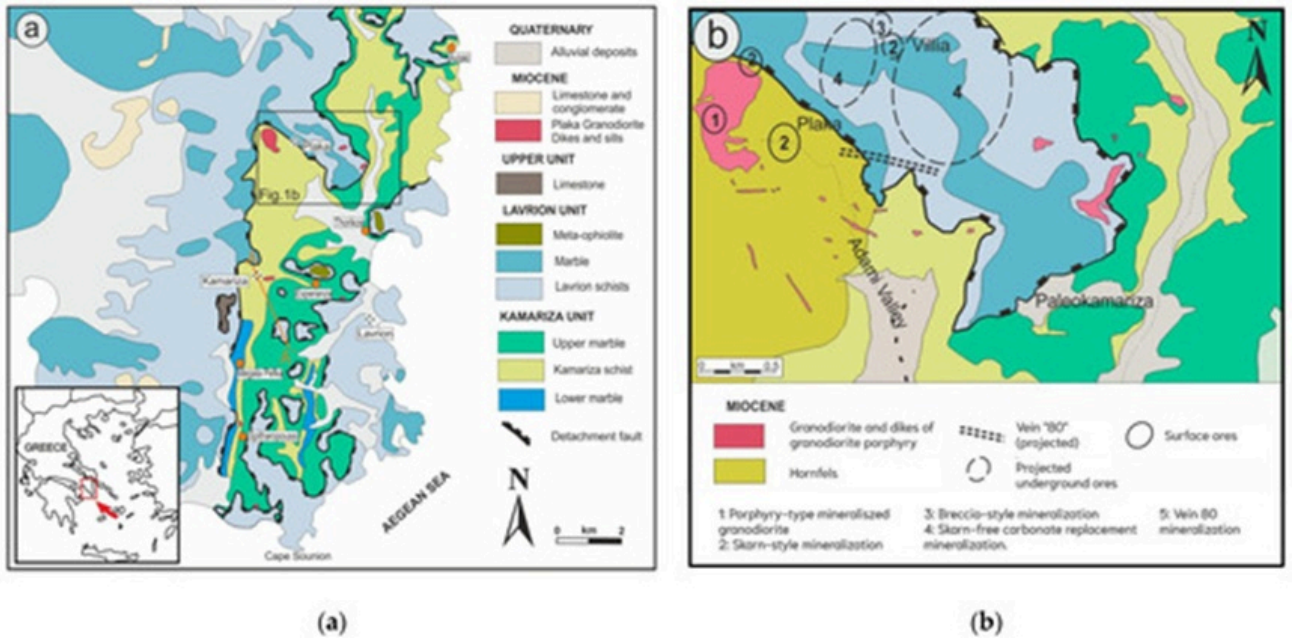

Figure 1. Geological overview: (a) Simplified geological map of the Lavrion ore district [22], and (b) Geological sketch map of the Plaka area [22].

A multitude of granitic and granodioritic intrusive forms, including laccolithic bodies, pipes, dikes, and sills, outcrop across the Lavrion district. Of these manifestations, the Plaka intrusive body **(Figure 1b)** stands out; it represents an I-type granodiorite enveloped by a broad contact metamorphism halo of calc–silicate hornfels developed within the Kamariza schists [23]. In conjunction with Kamariza, Plaka forms one of the principal mining localities within the broader Lavrion district.

A characteristic trait of the Lavrion orebody lies in its five separate but genetically intertwined ore-forming styles. These classifications incorporate (a) Mo-W porphyry-style, (b) Fe-Cu-Bi-Au skarn, (c) high-heat carbonate-replacement (non-skarn) Pb-Zn-Cu-Ag-Au deposition, and (d, e) Pb-Zn-Ag-Au fissure and breccia fill deposits [24]. With 672 catalogued mineral species, among them 25 type locality minerals, the Lavrion district harbors the richest tally of discrete mineral kinds known in any global mining territory [25]. This attribute transforms Lavrion into a priceless open-air laboratory for geological, mineralogical, and geochemical inquiry, providing researchers with an almost boundless domain of study and optimal learning environments. Additionally, the inclusion of Lavrion's mineralogical, geological, archaeological, and metallurgical landmarks in the UNESCO Global Geoparks scheme [26] safeguards its geological and cultural heritage, advances educational initiatives, and supports sustainable development.

Materials and Methods

Drone platform

The engineering of a bespoke UAV requires a rigorous, carefully organized strategy for material selection and design methodology, one that supports the broader goals of flexibility and multipurpose functionality. This segment delineates the operational aims set for the UAV. The approach adopted across both the conceptualization and detailed engineering stages strictly followed the framework detailed by Perikleous *et al.* [27]. Blending state-of-the-art technologies with judicious material selection proves essential for the UAV to dynamically reshape its configuration and role.

Operational objectives

© 2022 The Author(s). | Published by Agro Intelligence Research Press

Durability objectives: Thanks to its undercarriage assembly, the CERBERUS UAV is built to take off from and land on a range of ground conditions, including gravel, bare earth, grassy surfaces, and snow. It is designed to withstand wind speeds up to 6 on the Beaufort scale (6 bft) while maintaining its position. Airborne persistence varies according to the carried load; nonetheless, a typical mission yields a mean flight window of 35–40 min.

Performance objectives: The all-up mass of the platform at lift-off, including the affixed payload, has been determined to remain below the 25 kg threshold, in alignment with the A3 open category defined by the EASA Unmanned Aircraft Regulations [28]. The craft is engineered around the common principle that the peak propulsive force available from each motor must equal or surpass twice the force required to sustain hover. Upholding this requirement strengthens operational security by supplying a thrust reserve deployable under adverse atmospheric conditions or unforeseen circumstances, such as violent gusts or abrupt course changes. More concretely, the platform's gross weight, including payload, is 10.5 kg, while the total peak motor thrust is 22.8 kg. Hence, an excess of 50% of the total propulsive capacity stays on hand during flight.

Design objectives: The platform's physical proportions were fixed after considering the ideal clearance between adjacent rotors, a guideline stating that the inter-propeller gap should be roughly 18% of the propeller span [29]. Sizing the craft according to this metric aimed to enhance its functional performance while ensuring stable, dependable air operations. The drone assumes the most compact form possible to accommodate all vital apparatus. Its total span (the separation between two opposed motors) is 1.25 m, a figure dictated by the propeller dimensions, which here measure about 40 cm.

Technological objectives: The prototype embeds fundamental drone health-surveillance functions, including energy status indication, battery condition, and WiFi antenna connectivity, alongside higher-level flight and data-link features. Specifically, throughout a mission, it is capable of monitoring and controlling key flight phases such as departure, forward flight, and arrival, plus executing pre-scripted autonomous route scenarios. An ancillary onboard processing unit is also available for integration into the UAV should the need arise.

With respect to global positioning, the UAV used in this investigation requires the highest-precision geopositioning. To meet this demand, the H-RTK F9P, a high-fidelity GNSS receiver series from Holybro (Holybro, Hong Kong, China), was deployed. This unit supports multi-band RTK with rapid ambiguity-resolution intervals and dependable behaviour. It facilitates simultaneous lock-on to GPS (L1C/A and L2C), GLONASS (L1OF and L2OF), Galileo (E1-B/C and E5b), and BeiDou (B2a) constellations. It delivers a swift refresh cycle, making it well-suited for highly kinetic, data-intensive tasks that require precision at the centimetre scale.

Drone layout design and prototype

To portray the drone's structural arrangement, the authors draw on SOLIDWORKS 2024, a pre-eminent computer-aided design (CAD) and computer-aided engineering (CAE) software package widely used by designers worldwide. This capable tool enabled the generation of an exhaustive and intricate three-dimensional representation, serving as the basis for the novel drone architecture engineered.

Frame: The drone's structural chassis comprises two planar carbon fibre sheets **(Figure 2a)** and four arm-connection brackets **(Figure 2b)**, which serve as both load-bearing chassis members and arm connections. Aluminium pillars have been installed at strategic nodes to enhance overall structural integrity. Cut-outs and perforations have been provided to simplify component attachment and conductor management. Lastly, all onboard electronics are sealed within a tailor-made Carbon Fiber-Reinforced Plastic (CFRP) enclosure **(Figure 2c)** to safeguard the internal hardware further.

© 2022 The Author(s). | Published by Agro Intelligence Research Press

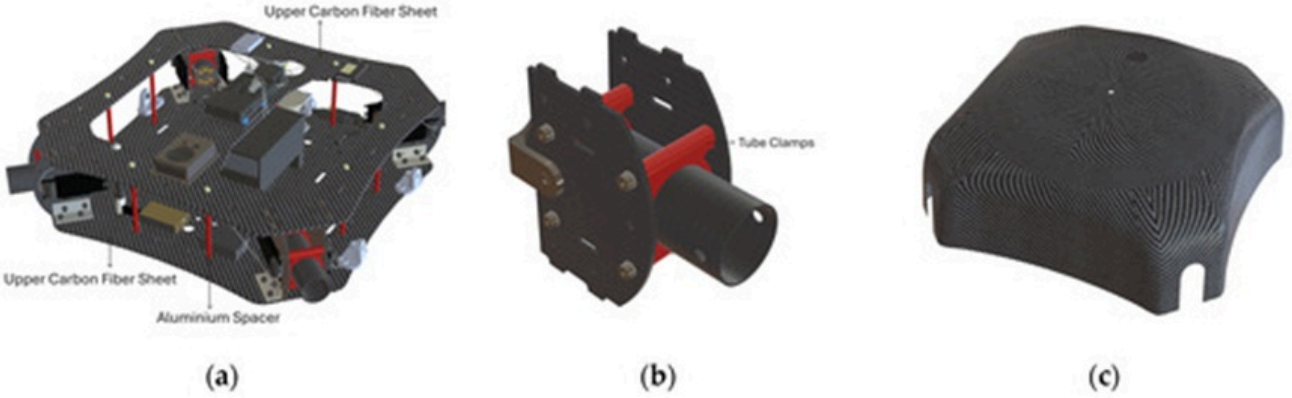

Figure 2. UAV 3D designs. (a) UAV frame; (b) arm mount; (c) UAV cover.

The technical illustrations in **Figure 2** were prepared for fabrication on a CNC routing table. The CFRP enclosure was shaped using a moulding technique and cured at elevated temperature under vacuum conditions (vacuum bagging). The finished product appears in **Figure 3**.

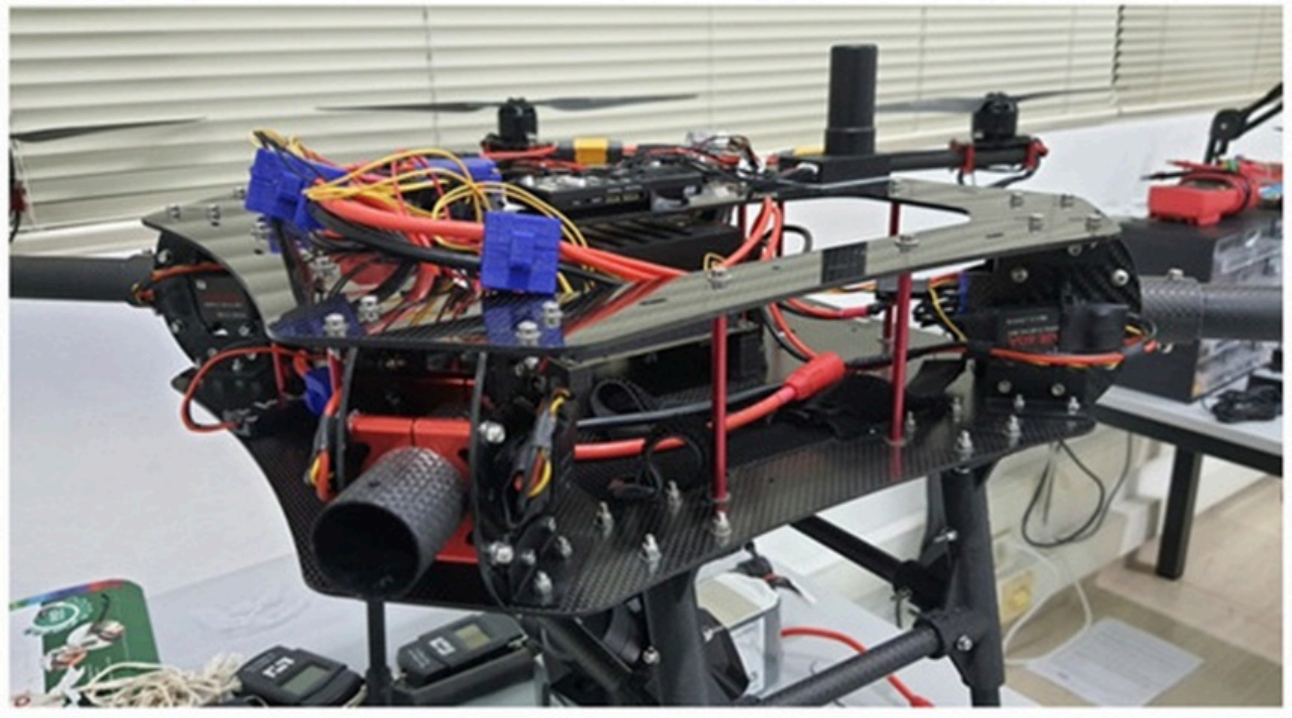

Figure 3. Manufactured UAV frame.

Arms with motors and propellers

The platform's chassis is equipped with four booms, each equipped with a bifurcated joint that holds two motor–propeller combinations on a single arm, as illustrated in **Figure 4**. This architecture enables the airframe to carry a total of eight motor–propeller combinations. The booms are designed to disconnect easily to reduce stowed dimensions and ease the craft's transport/storage during downtime.

© 2022 The Author(s). | Published by Agro Intelligence Research Press



Figure 4. Arms with motors and propellers: (a) 3D designed, and (b) prototype manufactured.

For the booms, carbon fibre tubing was cut and machined. The bifurcated joint, positioned at the midpoint of the boom arrangement, was designed in a CAD workspace and manufactured via additive manufacturing to link the three carbon fibre tubes.

The outer dimensional envelope of the CERBERUS prototype is given below **(Figure 5)**.

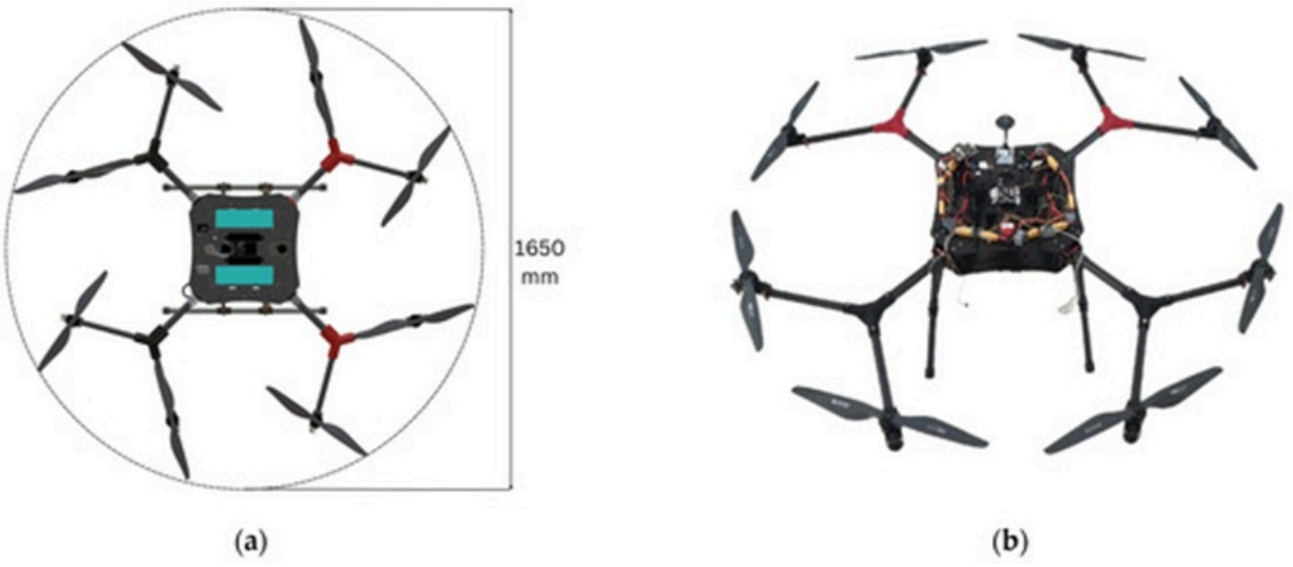

Figure 5. Frame and arms assembled: (a) 3D designed—top view, and (b) manufactured—top view.

Landing gear

The ground-contact assembly was conceived to meet the subsequent criteria:

• Furnish a firm and shock-mitigating platform for the drone.

• Assure uncomplicated and safe departure and arrival sequences for the drone.

The carbon fibre tubes were cut and drilled in conformity with the design. The connectors were additively manufactured, and stainless-steel threaded fasteners were used to bind them, forming the ground-contact assembly, as shown in **Figure 6**.

© 2022 The Author(s). | Published by Agro Intelligence Research Press



Figure 6. Landing gear: (a) 3D designed—trimetric view, and (b) manufactured—trimetric view.

Completed drone assembly

Ultimately, every electronic module, power conductor, and signal harness was placed in its allocated location together with the sub-assemblies noted in the preceding paragraphs. The finished product is visible in **Figure 7**.



Figure 7. CERBERUS UAV: (a) 3D designed, and (b) Manufactured.

System requirements and technical specifications

The tabulations provide a comprehensive overview, including the UAV's system requirements **(Table 1)** and its technical layout characteristics **(Table 2)**.

Table 1. UAV system requirements.

Requirements	Description
Nominal battery voltage: 22.2 V	Two 6S LiPo batteries connected in a parallel configuration (2 × 6S LiPo).
Battery charger	Charger capable of simultaneously charging two LiPo batteries, supporting up to 6S configuration.

© 2022 The Author(s). | Published by Agro Intelligence Research Press

Radio transmitter for manual piloting	Handheld radio transmitter compatible with the onboard autopilot system, used for manual flight control and monitoring power consumption.
Ground station	A ground control setup is required for both pre-flight preparation and in-flight operation and execution.

Table 2. UAV technical specifications.

Parameters	Description
Max diameter	1.65 m
Weight (no payload)	9.5 kg (airframe weight without any payload)
Maximum payload weight	5 kg (maximum allowable carried payload)
Expected flight time	35–40 min (anticipated endurance per flight)
Total motor thrust (100%)	22.8 kg (combined thrust output at full throttle)

Comparing the CERBERUS prototype with commercially prevalent drones used in extractive industry roles, notably the DJI M300 [30], is unavoidable. The DJI M300 has a maximum take-off weight (MTOW) of 9 kg and a maximum payload of 2.7 kg, while CERBERUS offers a superior MTOW, allowing a payload capacity of 5 kg. Even when measured against drones of comparable capabilities used in magnetometry fieldwork, CERBERUS distinguishes itself through operational simplicity, delivering a plug-and-play paradigm with detachable booms and a landing apparatus that can sustain substantial loads. This characteristic makes it especially promising for upcoming near-surface geophysics techniques such as Ground-Penetrating Radar (GPR) or Gamma-Ray Spectrometry (GRS).

Contrary to ready-made solutions that foreground user convenience, CERBERUS also provides resilient attributes purpose-built for scientific exploration. Through its hardware expandability, support for an integrated processor, and architecture that revolves around open-source autopilot software, CERBERUS affords academic and field researchers remarkable adaptability and authority.

Ultimately, CERBERUS provides a multipurpose platform that enables users to adapt both the aircraft and its operating software for magnetic surveying missions and a wide variety of subsequent geophysical ventures.

Magnetometry

Magnetic prospecting surveys entail measuring the intensity of the Earth's magnetic field across the terrain surface at evenly spaced points along a set of parallel transects termed a survey line. Though a predominant share of the planetary magnetic field originates from deep within the Earth's core (>90%), the spatial arrangement of distinct materials, above all ferromagnetic substances, throughout the crust gives rise to localized anomalies in the ambient magnetic field that instruments can register.

The CERBERUS Prototype was furnished with an exceptionally lightweight potassium-vapour magnetometer, the GEM GSMP-35U (noise floor 0.0002 nT @ 1 Hz), incorporating an external GPS receiver to log geographic coordinates in concert with the magnetic readings, spanning a dynamic range of 20,000 to 120,000 nT. The sensing head was deployed free from any rotational limitation along any axis.

The survey configuration and logging parameters were set as follows: measurement transects were oriented parallel to one another, with a maximum interline separation of 10 m. At the same time, the airborne velocity was maintained at 5 m/s. Information was captured at a temporal resolution of 100 ms, translating to 10 readings per second. A steady flight altitude relative to the local topography was maintained using a high-resolution digital terrain model previously

© 2022 The Author(s). | Published by Agro Intelligence Research Press

constructed from UAV-mounted LiDAR at a ground sampling resolution of 10 cm. The flight vehicle was kept at an altitude of 10 m, with the sensing head 7 m above the terrain. The flight corridor was laid out in advance, following a northwest–southeast alignment. The survey grid and the executed flight trajectories are summarized in **Table 3**.

Table 3. Characteristics and design of the flight area.

Area (Ha)	Separation between lines (m)	No. lines	Flight speed (m/s)	Sampling interval (ms)	Sensor height (m)
1.9	10	12	5	100	7

The system's constituent parts include a lightweight, highly sensitive magnetometer, a connecting electrical cable, and a sensor electronics enclosure, with the total system mass remaining below 1.0 kg. All necessary elements were firmly fastened and evenly balanced within the drone's undercarriage assembly **(Figure 8)**. To counteract electromagnetic disturbances from the platform's motors, the sensing instrument was positioned at a 3 m standoff beneath the drone's base, tethered by a cable, effectively neutralizing this contamination [11, 15, 17, 31-33]. In this setup, the drone's self-generated magnetic field is substantially weakened and does not distort the GSMP-35U magnetometer's readings. Nevertheless, a series of surface-level magnetic field measurements was performed at multiple drone-to-sensor distances to substantiate that the initial 3 m separation was indeed sufficient to eliminate signal interference. Moreover, given that the CERBERUS prototype represents an entirely new aerial platform, the drone underwent rigorous testing at the National Technical University of Athens. The evaluation comprised: (i) an initial test verifying that the drone's intrinsic magnetic interference falls within commercially acceptable boundaries; (ii) a subsequent test confirming that externally sourced magnetic disruptions do not compromise the drone's operational capabilities. Every test was executed using the same battery packs later deployed during the mining survey in Lavrion, Greece. It is worth noting that the power cells utilized throughout this work were LiPo batteries, whose construction relies chiefly on lithium salts, electrolytic compounds, and carbon-derived anodes—materials entirely devoid of ferromagnetic properties. The external housing of these LiPo cells is fabricated from plastic, an inherently non-magnetic substance.

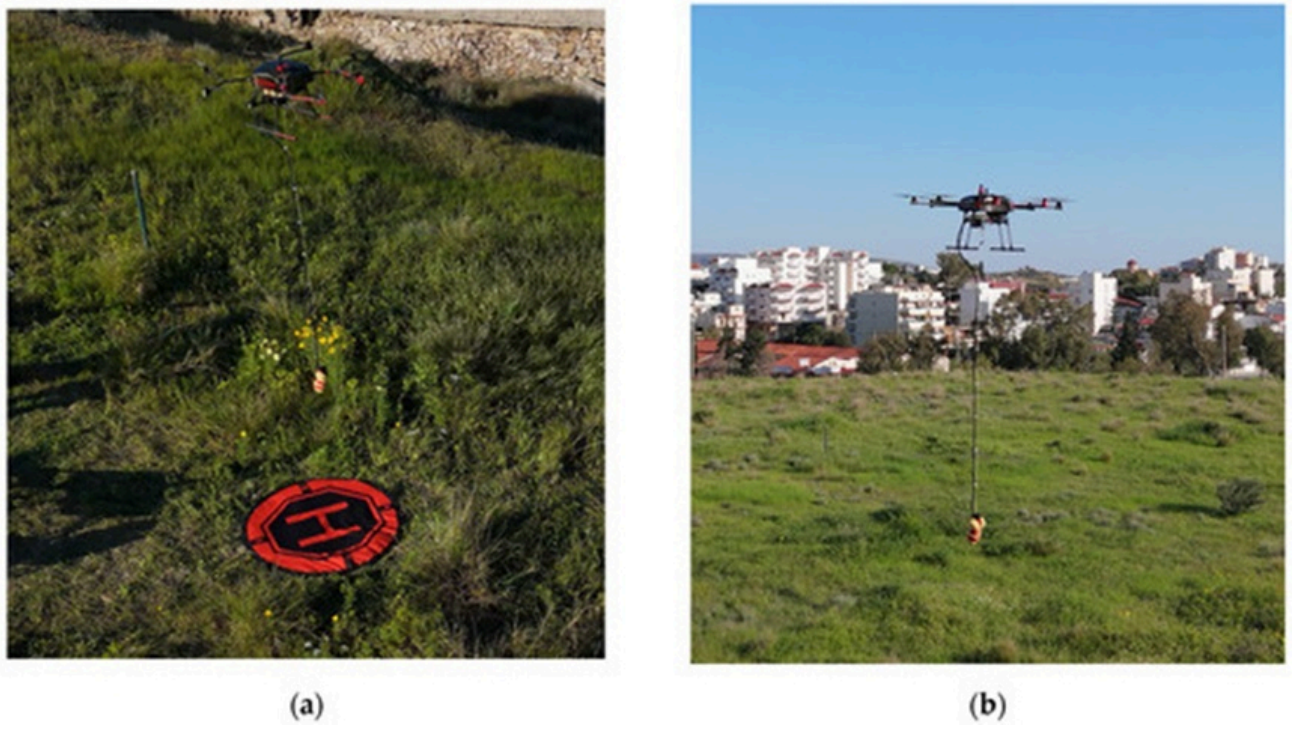

(a) (b)

© 2022 The Author(s). | Published by Agro Intelligence Research Press

Figure 8. CERBERUS UAV with the GSMP-35U magnetometer: (a) CERBERUS UAV take off, and (b) Field data collection. Bearing in mind the possible detrimental effect of poor weather on measurement quality, all survey sorties were flown under favourable atmospheric conditions **(Figure 8)**, thereby keeping sensor oscillations to a minimum.

Finally, throughout the acquisition phase, a fixed-base reference magnetometer (GSMP-35) was deployed at a neighbouring location, meticulously chosen to be free of magnetic disturbances. Its function was to continuously record and enable correction for the diurnal fluctuation of the Earth's magnetic field arising from temporal variations across the day. The instrument was programmed to register the total magnetic field intensity every 1 s, yielding precise readings for this adjustment. Synchronization between the base station magnetometer data and the UAV-carried magnetometer was achieved using a GPS time signal.

Processing and interpretation

The overarching goal of data processing is to distill meaningful information from raw field measurements to facilitate subsequent interpretation. The processing pipeline addresses signal artefacts unrelated to subsurface geology or mineralogy, which may stem from survey methodology, instrumental characteristics, external environmental factors, and time-dependent variations. Collectively, these can't "taint" the recorded signal. To tackle these issues, a sequence of mathematical filters was applied to isolate and present data relevant for geological interpretation. To begin with, spurious readings associated with the drone's positioning—encompassing the departure, arrival, and banking manoeuvres required to line up with each survey transect—were eliminated. Following this, the diurnal magnetic variations were compensated for, after which the airborne quality control module in OASIS Montaj 2024.1 was used to scrutinize and remove potential noise from the dataset. During this examination, the data were inspected for heading-dependent errors; none were detected.

The handling of the aeromagnetic dataset was accomplished through an interpolation procedure that organized the observed readings into a regularly spaced grid. The resultant grid nodes were visualized as a 2D contour representation of the total magnetic intensity (RGB image). For the present study, the minimum curvature gridding algorithm was utilized, configured at a resolution of one quarter of the flight line separation (10 m), yielding a grid cell size of 2.5 m. After the foundational data treatment, further filtering operations were performed to segregate and extract anomaly signatures associated with specific geological, structural, mineralogical, and depth-related attributes. All data manipulation and processing tasks were performed within dedicated geomagnetic survey software environments (GemLink 5.4 and OASIS Montaj 2024.1). The culmination of these filtering procedures is the derivation of assorted profiles and magnetic signal models characterizing the surveyed repository. As will be elaborated in subsequent sections, these preliminary datasets can also serve as inputs for generating three-dimensional representations of the repository using specific inversion algorithms [34, 35]. This involves constructing a mathematical formulation that reproduces the magnetic response of various subsurface configurations and iteratively adjusting it to minimize the misfit between the observed measurements and the simulated magnetic data. In particular, the implemented approach combines Tikhonov regularization with a least-squares inversion scheme.

The final phase encompasses the geological interpretation of the findings, a task typically underpinned by the available background knowledge and the interpretive skill cultivated by the geophysicist through prior engagements in analogous settings. The complete sequence of stages and processes is consolidated in **Figure 9**.

© 2022 The Author(s). | Published by Agro Intelligence Research Press

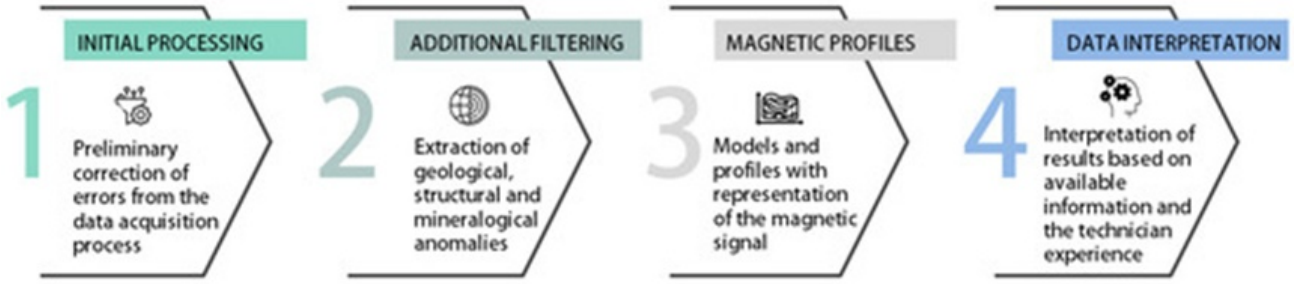

Figure 9. Drone-based magnetometer data processing workflow.

Results and Discussion

To support the interpretation of the outcomes derived from the magnetic geophysical campaign, a concise overview of material behaviour is presented, covering ferromagnetic, antiferromagnetic, paramagnetic, and diamagnetic categories. For a more extensive treatment, readers are encouraged to consult [36, 37]. **Figure 10** presents a periodic table of the elements, classifying them by magnetic susceptibility type, whereas **Table 4** lists the metals identified in the repository along with their respective magnetic susceptibility magnitudes.

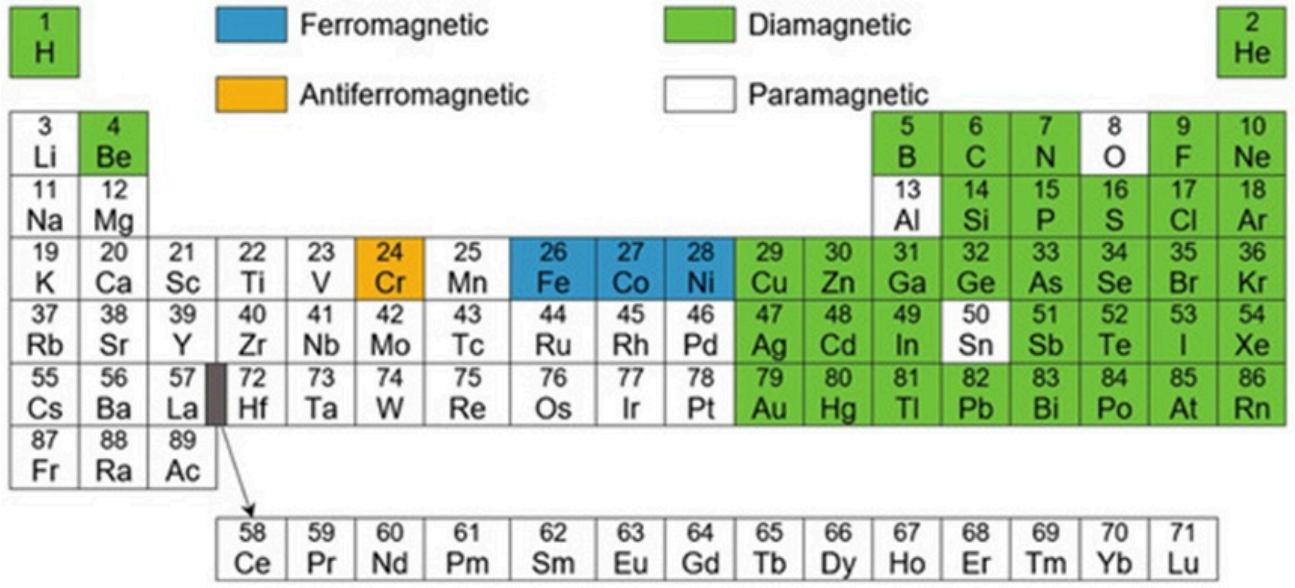

Figure 10. Magnetic properties of the elements.

Table 4. Average metal and metalloid concentrations (mg kg−1) in the Repository of Lavrion (Greece) and magnetic susceptibility (SI). Ferromagnetic elements such as Ni and Fe do not have specified magnetic susceptibilities because their susceptibilities are extremely high and vary significantly with external factors, such as material composition, temperature, and structure, rendering them non-constant. This contrasts with diamagnetic, paramagnetic, and antiferromagnetic materials, whose susceptibility values are relatively constant and predictable under standard conditions.

Element	Average concentration	Maximum concentration	Magnetic susceptibility
Pb	32.430	67.700	Diamagnetic −0.000017

© 2022 The Author(s). | Published by Agro Intelligence Research Press

As	4.517	10.800	Diamagnetic −0.0000223
Cd	160	600	Diamagnetic −0.0000199
Cr	4	10	Antiferromagnetic 0.0003177
Ni	150	300	**Ferromagnetic**
Zn	47.843	97.900	Diamagnetic −0.0000158
Mn	9.002	16.600	Paramagnetic 0.00090387
Fe	154.800	275.200	**Ferromagnetic**
Cu	2.548	6.300	Diamagnetic -9.63×10^{-6}

Total Magnetic Field (TMF)

The figure below **(Figure 11)** presents the layout of the magnetic survey results collected over the investigated site. The measurements show pronounced contrasts across the repository materials, as inferred from the magnetic field response, suggesting the presence of regions with differing compositional makeup. Nevertheless, the surveyed terrain did not yield evidence of any notable magnetic dipoles indicative of sizeable magnetized bodies.

© 2022 The Author(s). | Published by Agro Intelligence Research Press

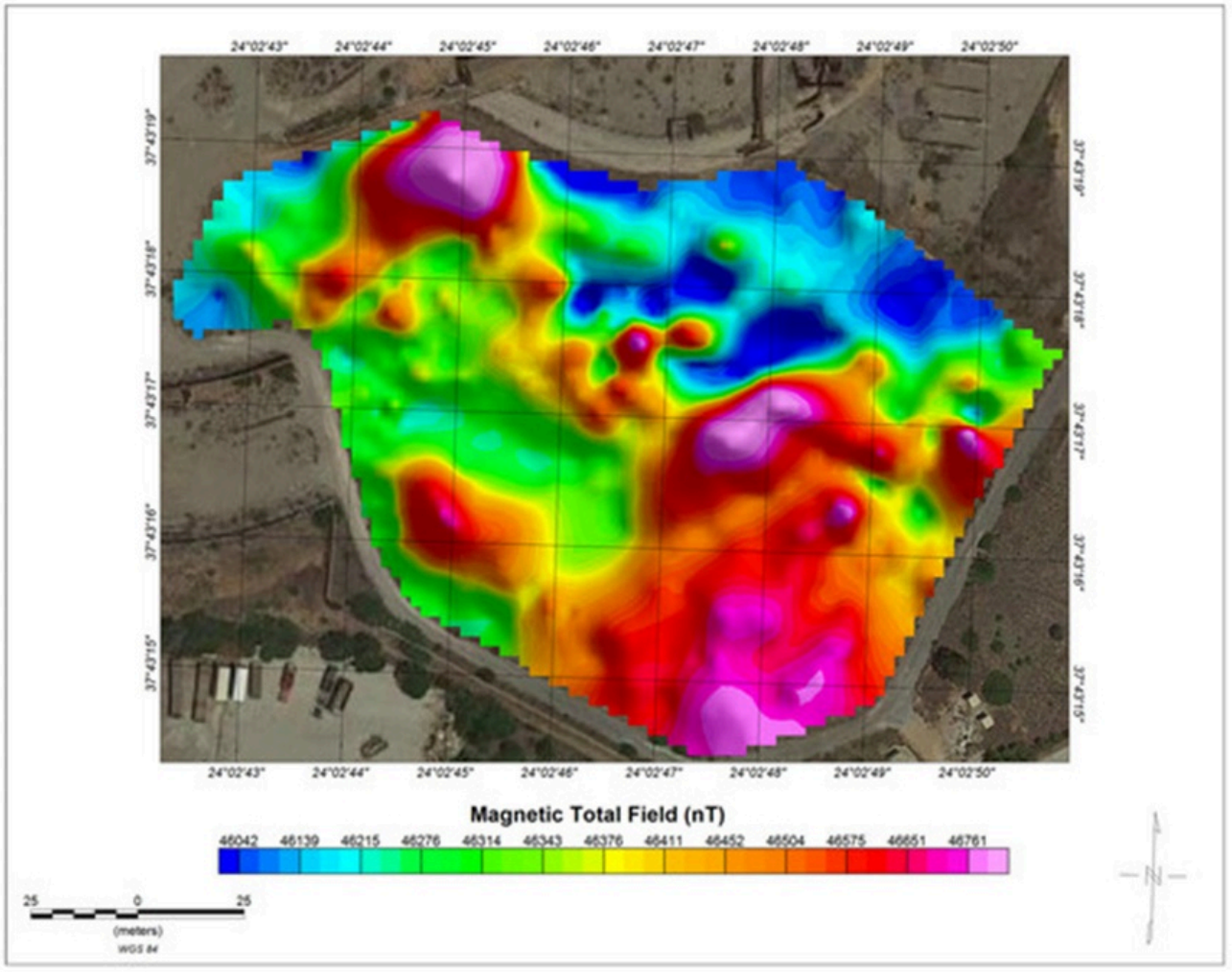

Figure 11. Total magnetic field (coordinate reference system—CRS: WGS84). Despite the visual impression of smoothing in the dataset, no smoothing filtering was undertaken in this work. A screening procedure leveraging the OASIS Montaj' airborne quality control' module was run to detect potential heading errors, and none were present. It should also be noted that a potassium-type magnetometer served as the primary sensor, a class of instrument known to exhibit reduced sensitivity to heading errors in comparison with other designs, such as proton magnetometers [38].

The prospecting effort identified patches of varying magnetic strength, a pattern that indicates contrasts in the chemical composition or typology of near-surface materials. Specifically, lead (Pb), arsenic (As), cadmium (Cd), zinc (Zn), and copper (Cu) comprise the principal diamagnetic species in this repository. Although their abundances are far from uniform, these elements are expected to supply only a marginal input to the aggregate magnetic field, and consequently do not give rise to any sizeable magnetic disturbances or dipoles. The substantial cadmium loading (averaging 160, with maxima nearing 600) merits attention; however, the element's weakly diamagnetic character precludes it from generating a forceful magnetic expression. Chromium (Cr) holds a barely positive magnetic susceptibility as a consequence of its antiferromagnetic ordering. At the low abundance range encountered (mean of 4, upper bound of 10), chromium could be responsible for faint magnetic undulations. With respect to ferromagnetic species, both nickel (Ni) and iron fall into this category and accordingly exert a dominant influence on magnetic field readings, reflecting their highly positive susceptibilities. Nickel is found at a moderate abundance level (averaging 150, peaking at 300), a range capable of producing restricted magnetic perturbations. Iron (Fe), documented at a high mean abundance (154.8, extending to 275.2), is presumed to be the foremost agent behind the magnetic variability captured by the survey. The ferromagnetic response of iron makes it readily detectable by magnetic methods, which plausibly explains the compositional zonation

© 2022 The Author(s). | Published by Agro Intelligence Research Press

observed. Despite these abundance figures, the absence of pronounced dipoles in the dataset indicates a lack of sufficiently concentrated accumulations of metallic iron or nickel to yield discrete magnetic expressions. This points to a model in which iron and nickel, though undeniably present, are dispersed. Shifting the focus to paramagnetic constituents, manganese (Mn) is characterized by a relatively modest magnetic susceptibility and a moderate abundance (mean of 9, maximum of 16.6). Its capacity to shape the overall magnetic field is minor compared to the ferromagnetic contributions of iron and nickel.

Magnetic Field Reduction to the Pole (MFRP)

The reduction-to-pole operation, as utilized in magnetic surveying, mathematically shifts anomalies measured at ground level to their equivalent form as though acquisition had occurred at the north magnetic pole. The transformation strips away the distorting effects tied to the Earth's field inclination and declination, enabling each anomaly to be read under the assumption of a vertical inducing field. This correction renders anomalies symmetric and centred squarely above their subsurface origins, thereby streamlining the task of pinpointing and characterizing buried magnetized targets through a less ambiguous portrayal of their spatial arrangement.

The Reduction to Pole (MFRP) representation **(Figure 12)** shows only slight divergence from the total magnetic field (TMF) data, with a dynamic range of about 1000 nT between the minimum and maximum readings. Nonetheless, the outcome continues to underscore meaningful magnetic heterogeneity throughout the repository interior, consistent with the presence of compositionally distinct domains.

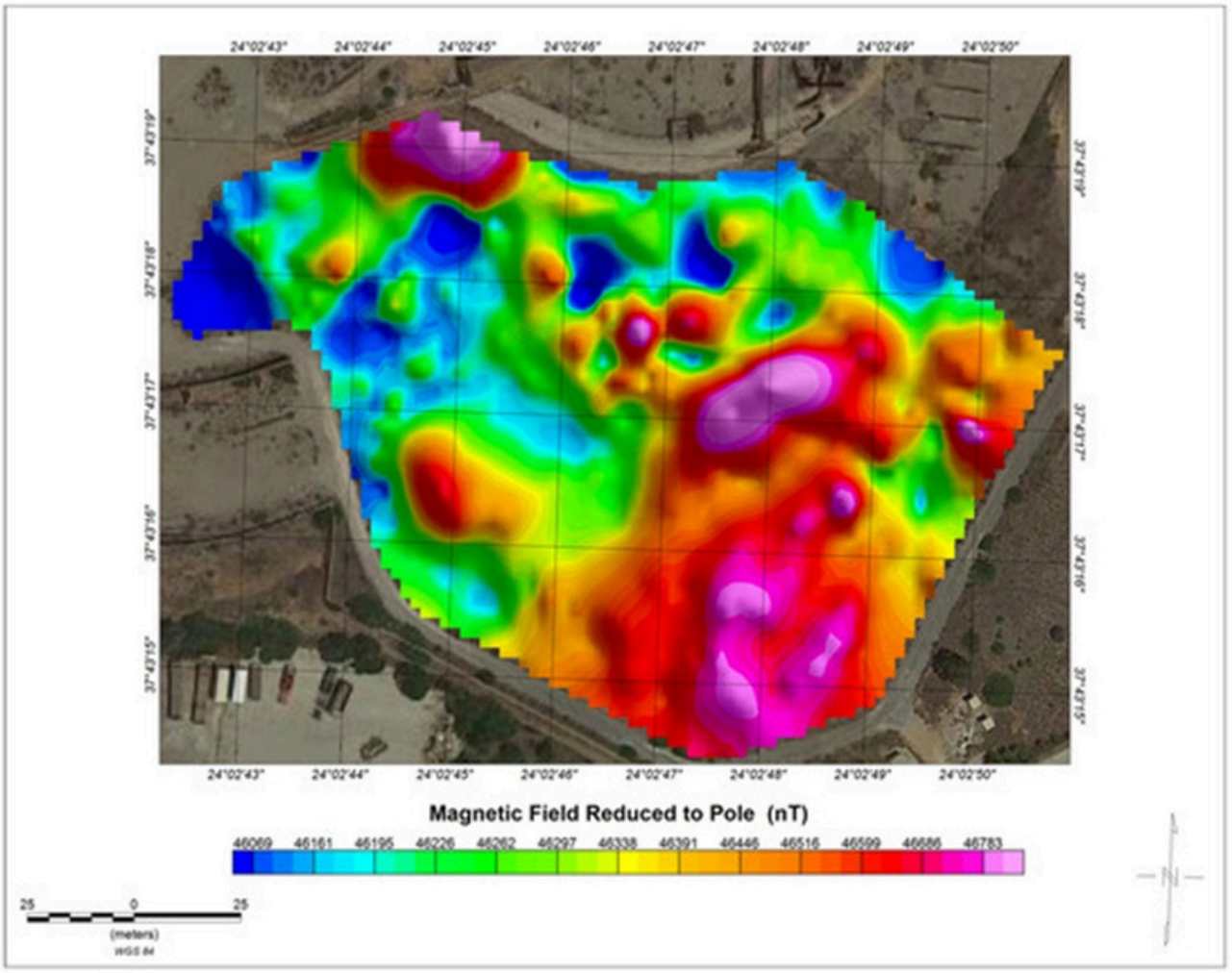

© 2022 The Author(s). | Published by Agro Intelligence Research Press

Figure 12. Total magnetic field reduced to pole (CRS: WGS84).

Analytical Signal (AS)

The analytical signal transformation is used to amplify magnetic anomalies relative to the broader regional field, thereby highlighting those values that depart from the site's averaged magnetic background **(Figure 13)**. As shown in the image, the most energetic magnetic responses are concentrated in the northeastern quadrant of the repository. This pattern suggests that the sector in question supports a comparatively higher loading of magnetic material than the remainder of the surveyed area. Given documented susceptibilities and elemental abundances, iron (Fe), together with perhaps nickel (Ni), is likely the source powering these amplified anomalies. The ferromagnetic nature of both metals enhances their visibility in magnetic datasets and, consequently, their stronger expression in the analytical signal. The clear demarcation of this feature against the background indicates that. In contrast, magnetic phases may be distributed diffusely elsewhere; the northeastern zone encloses a localized enrichment, potentially reflective of a discrete disposal episode or a unique chapter in the site's infill history.

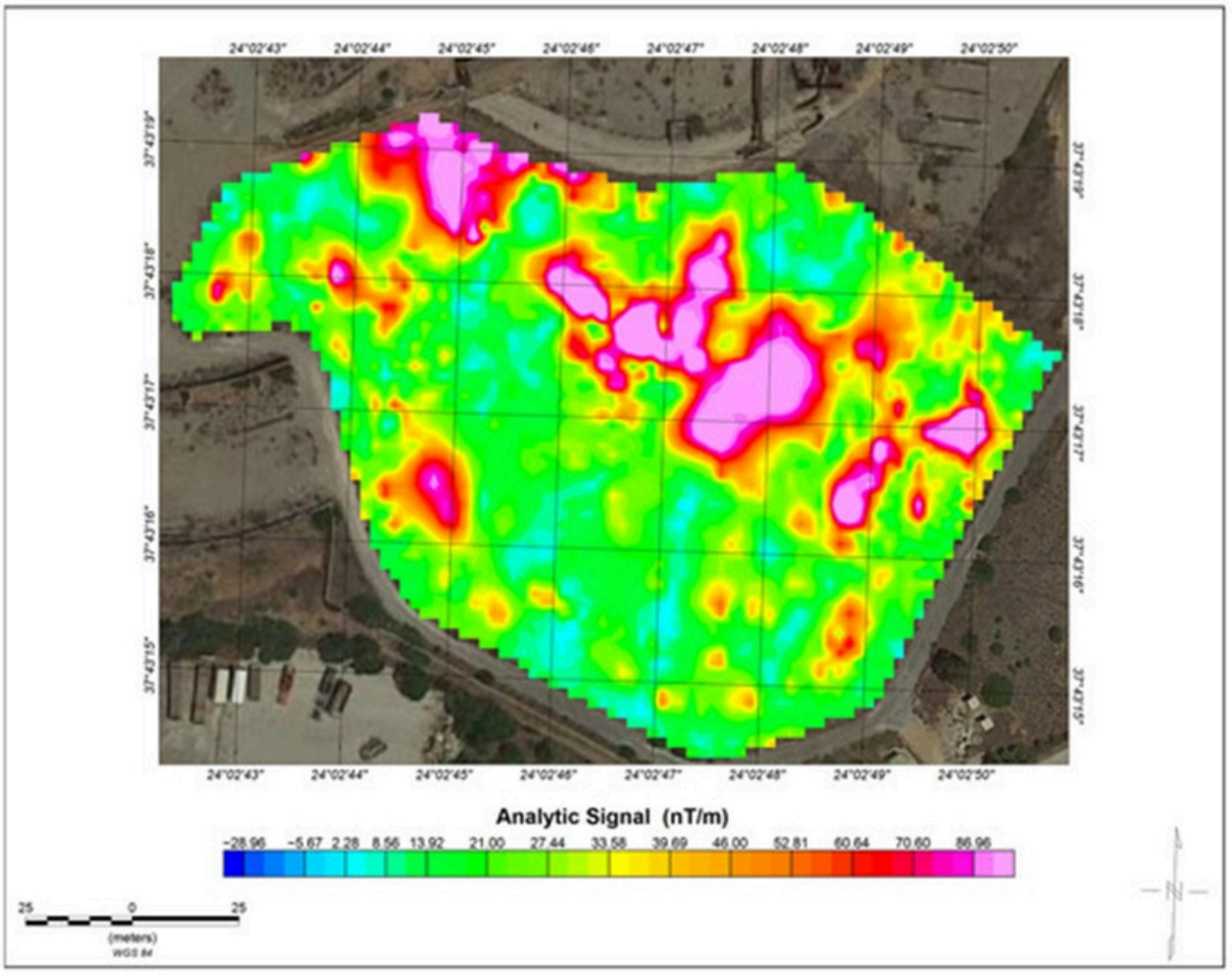

Figure 13. Analytic signal (CRS: WGS84).

TILT Derivative (TD)

The TILT derivative **(Figure 14a)** reveals the boundaries separating rock volumes or fill units of contrasting magnetic character, which correspond to discontinuities in material composition. Formulated to accentuate the edges or contact

© 2022 The Author(s). | Published by Agro Intelligence Research Press

surfaces between zones of dissimilar magnetic susceptibility, the TILT derivative proves effective at delineating transition or interface zones. The identification of these contact zones is a primary objective of the present study. The resulting map is especially instructive, uncovering a network of linear boundary features **(Figure 14b)** that attest to the co-existence of materials with disparate compositions across the repository. Such linear contact geometries suggest that the repository infill may follow a layered or compartmentalized architecture. This structural style could be the product of successive infilling stages, deliberate alternating of material types, or intrinsic inhomogeneity in the waste stream composition.

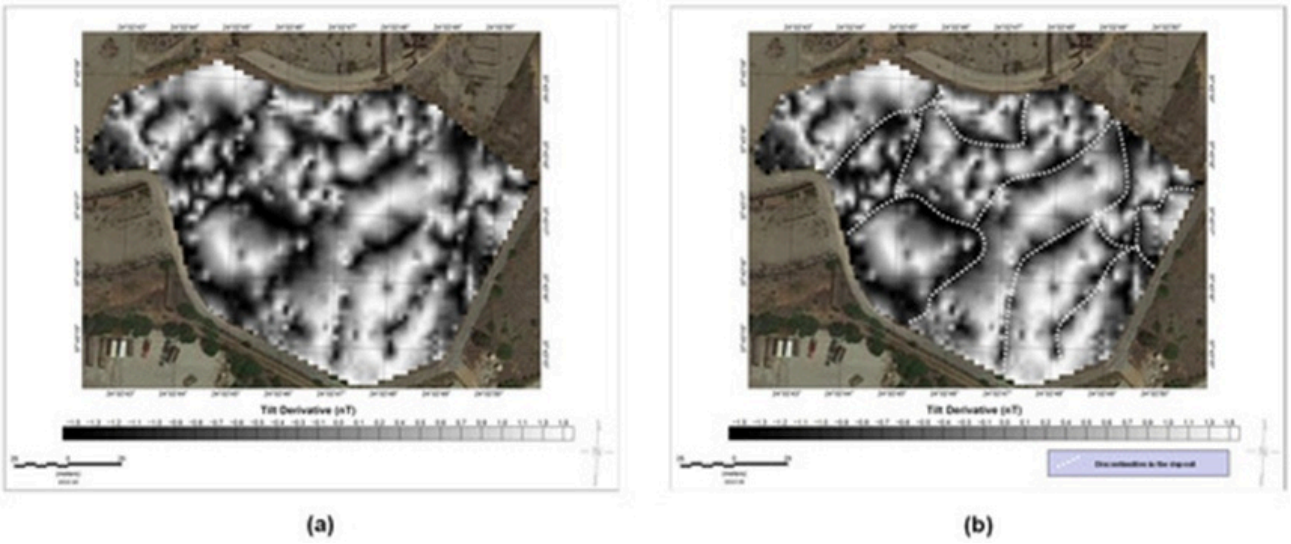

Figure 14. (a) TILT derivative (WGS84 35N); (b) Interpretation of TILT derivative (WGS84).

In a final analytical step, the pole-reduced magnetic field grid was draped over the TILT derivative plane **(Figure 15)**, enabling a sharper, more nuanced deconstruction of the various elemental associations in the repository. This fused visualization improves the capability to discern and evaluate the compositional fabric of the study area. As the composite image shows, the repository is partitioned into distinct compartments that exhibit different magnetic field intensities. Those compartments displaying elevated field values are most plausibly linked with pockets of heightened ferromagnetic material abundance, notably iron and nickel. A forthcoming 3D magnetic susceptibility model promises to lend additional resolving power to the interpretation of these datasets.

© 2022 The Author(s). | Published by Agro Intelligence Research Press

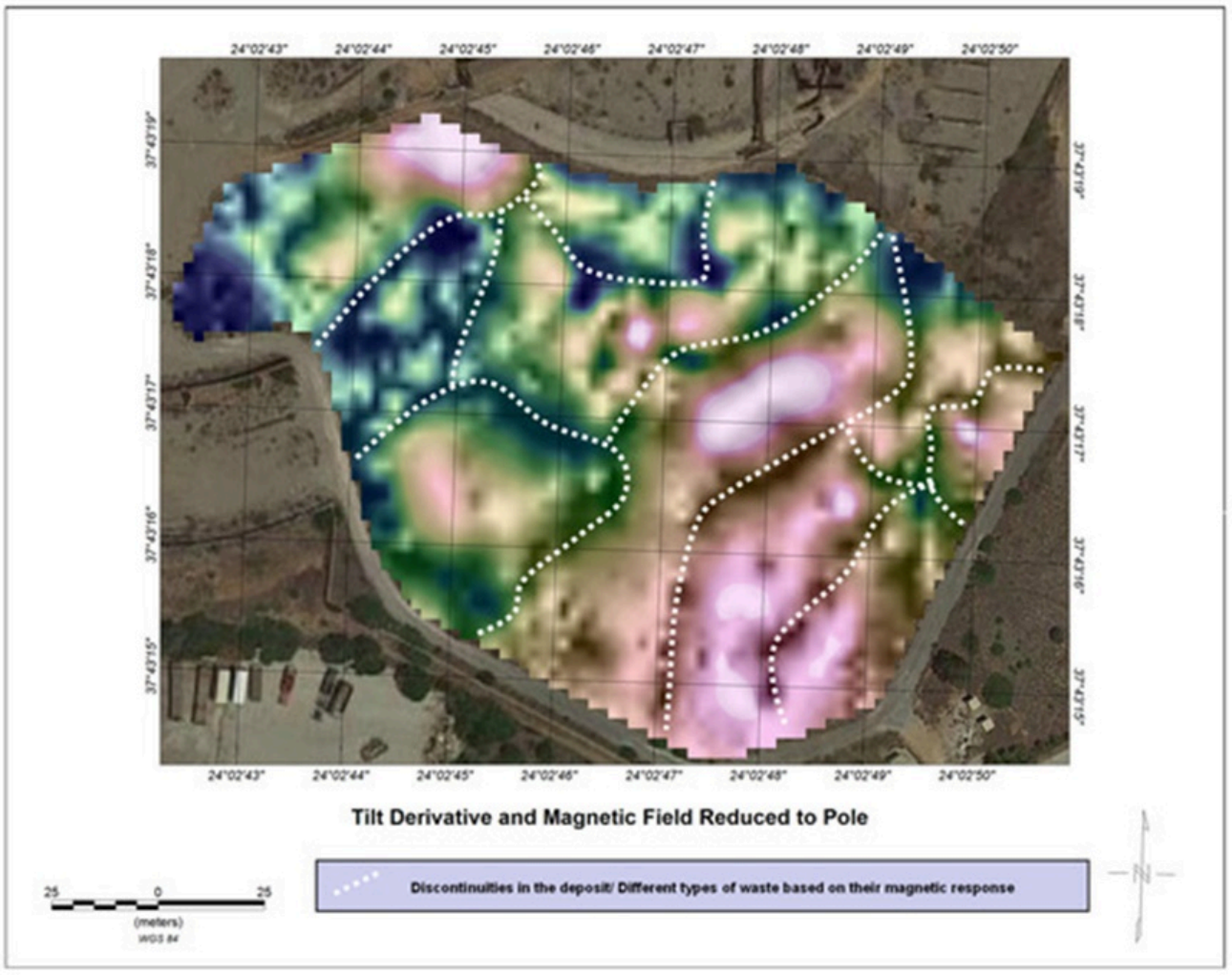

Figure 15. Interpretation of the TILT derivative and magnetic field reduced to pole (CRS: WGS84).

Given the suite of materials catalogued (with iron, nickel, and manganese qualifying as the magnetic carriers), these linear discontinuities likely mark transitions where ferromagnetic or paramagnetic assemblages give way to terrains underlain predominantly by diamagnetic species (typified by lead, zinc, and cadmium).

Pseudo Gravity (PG)

The pseudo-gravity filter **(Figure 16)** is a processing step applied during the magnetic assessment of the repository, in which magnetic anomaly patterns are mathematically recast into synthetic gravity signatures. The procedure exploits the theoretical relationship between a body's magnetic response and its gravitational field, assuming that the repository contains materials whose magnetization and density vary in tandem. By enacting this transformation, magnetic features are rendered as a gravimetric-equivalent image, offering a complementary perspective for distinguishing and classifying zones within the waste body. Such an approach enriches the picture of how the buried materials are distributed and constituted, ultimately strengthening the reliability of site supervision and long-term tracking.

© 2022 The Author(s). | Published by Agro Intelligence Research Press

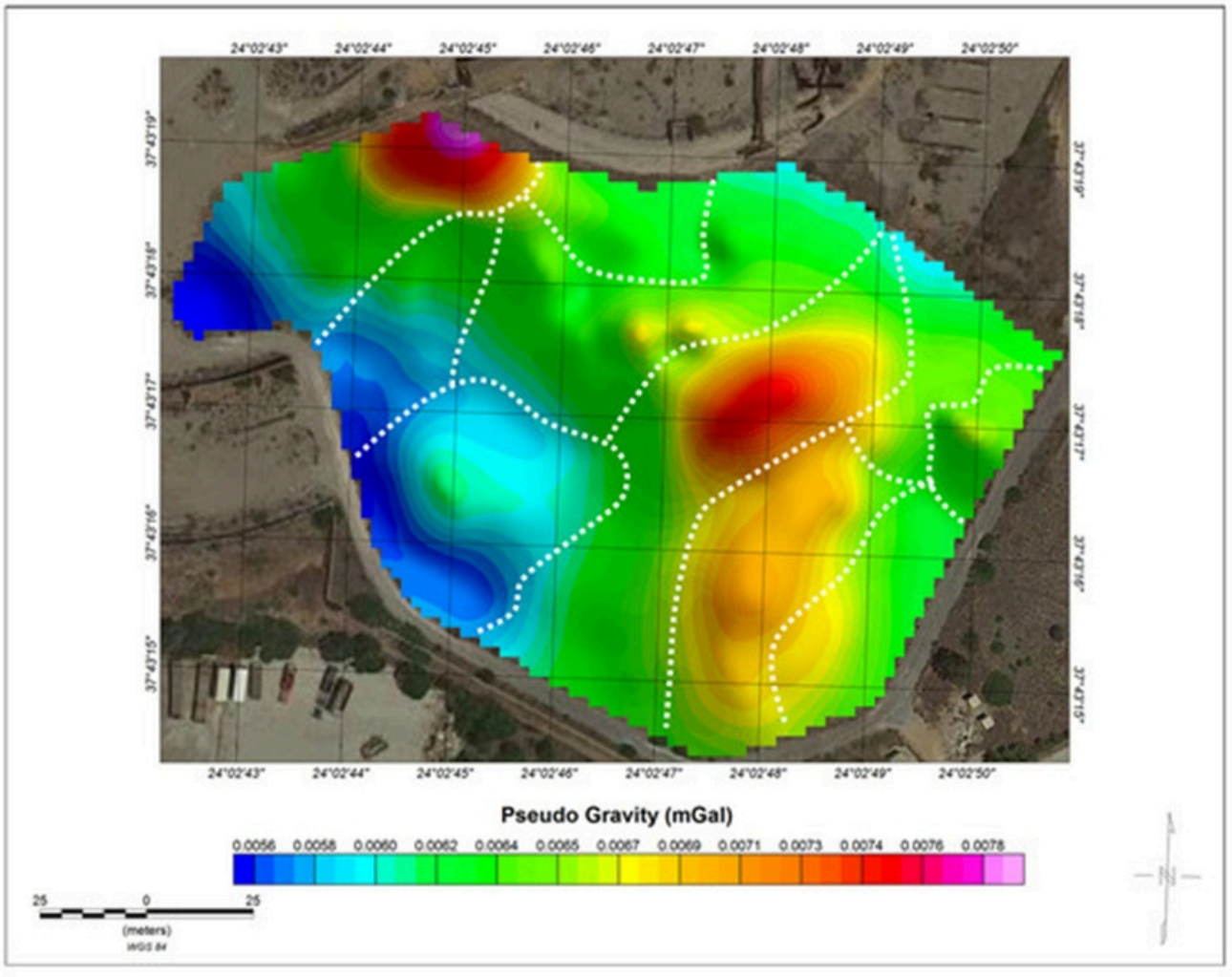

Figure 16. Pseudo gravity (CRS: WGS84).

As the output demonstrates, the highest pseudo-gravity and, therefore, the highest effective density values are recorded across the central, southeastern, and northwestern reaches of the repository. Taking into account the known material inventory of the site, it is reasonable to infer that high pseudo-gravity domains correspond to zones enriched in ferromagnetic species (iron and nickel being the prime examples), and perhaps also in other dense yet magnetically unresponsive substances that nonetheless carry appreciable mass. The pseudo-gravity product provides a supplementary information layer, particularly advantageous for teasing apart materials that share similar magnetic fingerprints but differ in density. Such a capability is especially valuable in a heterogeneous repository, where fluctuations in both magnetic susceptibility and density are to be expected given the variety of deposited materials. For instance, iron and nickel, which boost both the magnetic susceptibility and the density of their host volume, feature conspicuously in both magnetic and pseudo-gravity representations. By contrast, other dense components (such as potentially non-magnetic waste fractions) would manifest clearly in the pseudo-gravity rendition while remaining subdued or absent in the magnetic records alone, thereby enabling a more holistic inventory of the repository's contents.

3D Inversion model

The operational use of the CERBERUS platform has enabled the construction of a finely resolved, uniformly structured grid, which, in turn, has enabled the generation of three-dimensional volumes of magnetic susceptibility using state-of-

© 2022 The Author(s). | Published by Agro Intelligence Research Press

the-art inversion workflows. These volumes, built within the VOXI Earth Modelling package of the OASIS Montaj suite, have markedly simplified the process of recognizing and delimiting the spatial footprint of diverse magnetized units.

Using the collected magnetic measurements, a 3D magnetic susceptibility block model **(Figures 17-19)** was generated. The output volume contains 10,720 individual cells, each possessing a lateral footprint of 5 × 5 m **(Figure 17)**. The model's refined cell size ensures that even slight fluctuations in magnetic susceptibility are resolved, a prerequisite for pinpointing diminutive features or subtle, gradational shifts in material makeup. Such granularity facilitates the detection of both expansive magnetized zones and compact, localized disturbances that coarser representations might miss. The uniform gridding framework, for its part, provides robust spatial continuity, yielding an unbroken depiction of susceptibility trends that aids in deciphering subsurface fabrics and directional patterns.

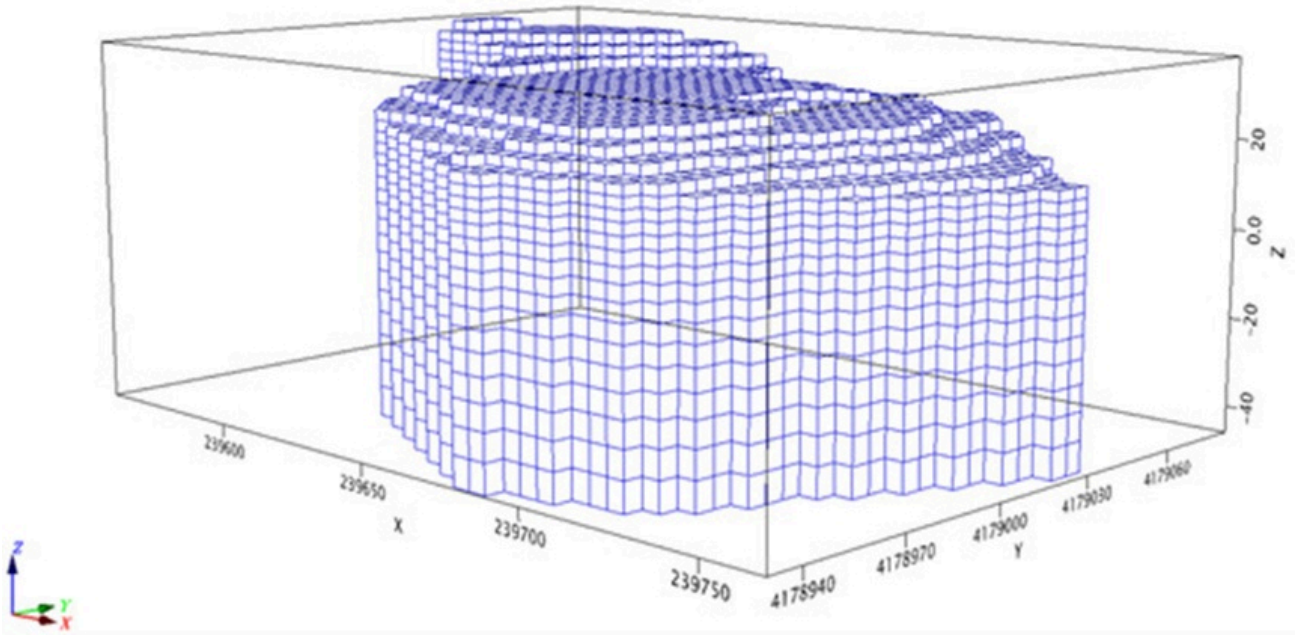

Figure 17. 3D magnetic susceptibility block model (CRS: WGS84 35N).

The sophisticated inversion methodology utilized here re-expresses the total field magnetic data into a configuration far easier to interpret, one in which susceptibility magnitudes map directly onto the density and character of magnetic mineral assemblages. This reformulation enables crisp boundary definition, in turn supporting spatially focused exploration and resource administration.

Performed within OASIS Montaj through the VOXI module, the magnetic inversion procedure converged to a remarkably close match between the field-observed and forward-computed magnetic response after 11 iterative refinements. The fit quality metric (DataFit) showed a significant improvement, falling from an initial 543.98 to a final 1.0201, paired with a well-constrained regularization term (RegScal).

Figure 18 displays the products of this inversion sequence: (a) the as-measured magnetic anomaly field, (b) the forward-predicted magnetic field synthesized from the inversion outcome, and (c) a residual grid (observed minus predicted) that exposes small-scale departure zones. The root-mean-square (RMS) value of 5.88 provides further quantitative evidence of the tight correspondence between empirical readings and modelled outputs. Collectively, these findings validate the model's fidelity in reproducing the true subsurface susceptibility architecture beneath the survey area.

© 2022 The Author(s). | Published by Agro Intelligence Research Press

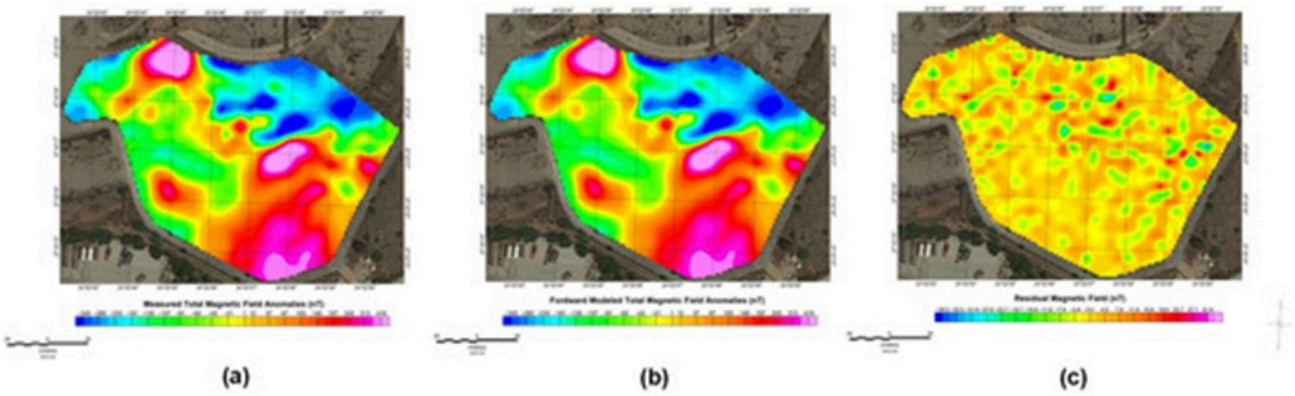

Figure 18. Comparison of measured and forward-modelled magnetic anomalies and their residuals: (a) Measured magnetic anomalies (nT) from UAV data, (b) Forward-modelled magnetic anomalies (nT) derived from the 3D magnetic susceptibility inversion, and (c) Residual magnetic field map.

The pair of figures that follow **(Figures 19 and 20)** supplies alternative visual perspectives of the finalized 3D magnetic susceptibility volume.

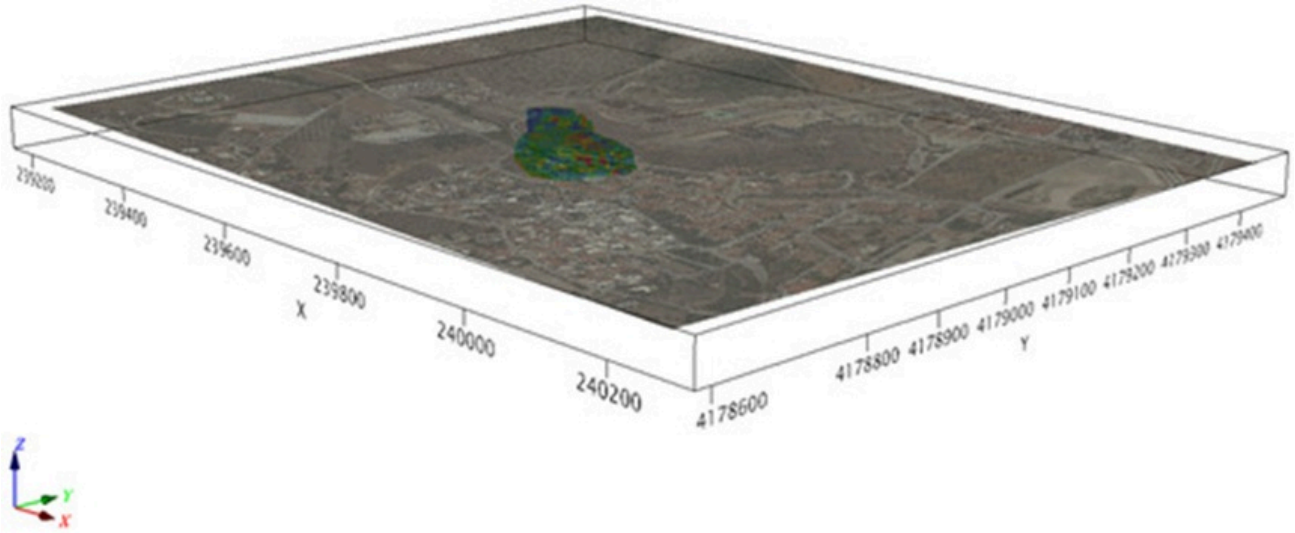

Figure 19. 3D magnetic susceptibility model with orthoimage (CRS: ETRS84 35N).

© 2022 The Author(s). | Published by Agro Intelligence Research Press

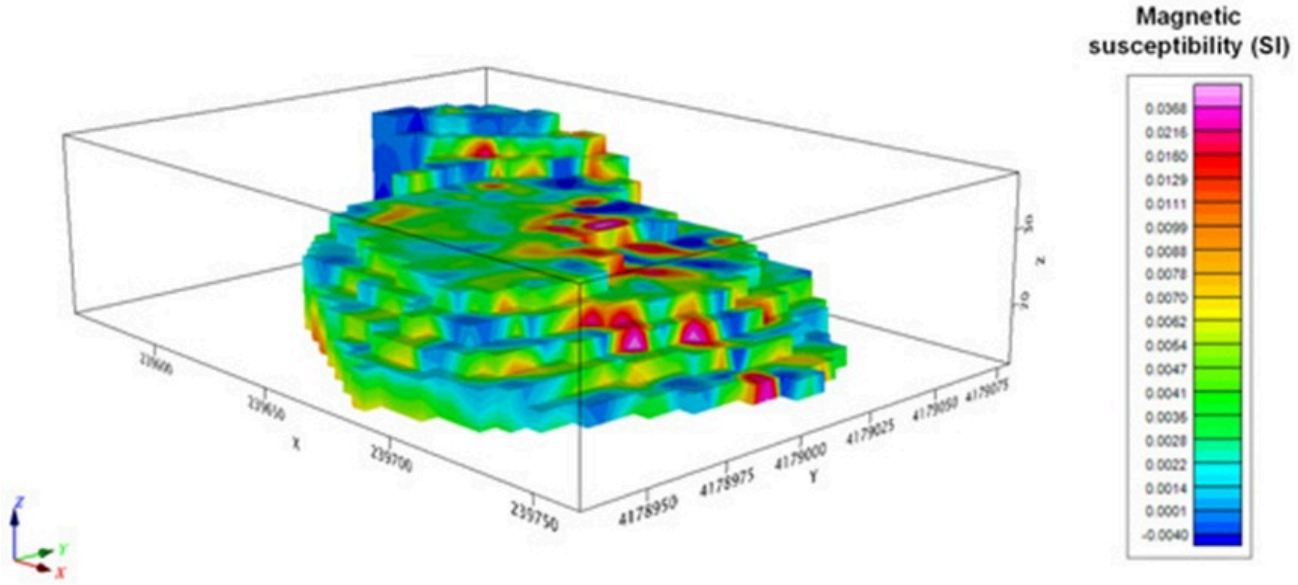

Figure 20. 3D magnetic susceptibility model with orthoimage (CRS: ETRS84 35N).

The three-dimensional reconstruction derived from the magnetic susceptibility parameter has furnished a geophysical portrait of the repository, capturing its internal arrangement in considerable detail **(Figure 21)**. From a compositional standpoint, the interpretation posits that peaks in susceptibility coincide with an enrichment of ferromagnetic phases, most notably iron and nickel. At the other end, subdued or negative susceptibility readings are taken to indicate regions where the ferromagnetic fraction dwindles, and diamagnetic carriers—lead, arsenic, cadmium, and zinc among them—become dominant.

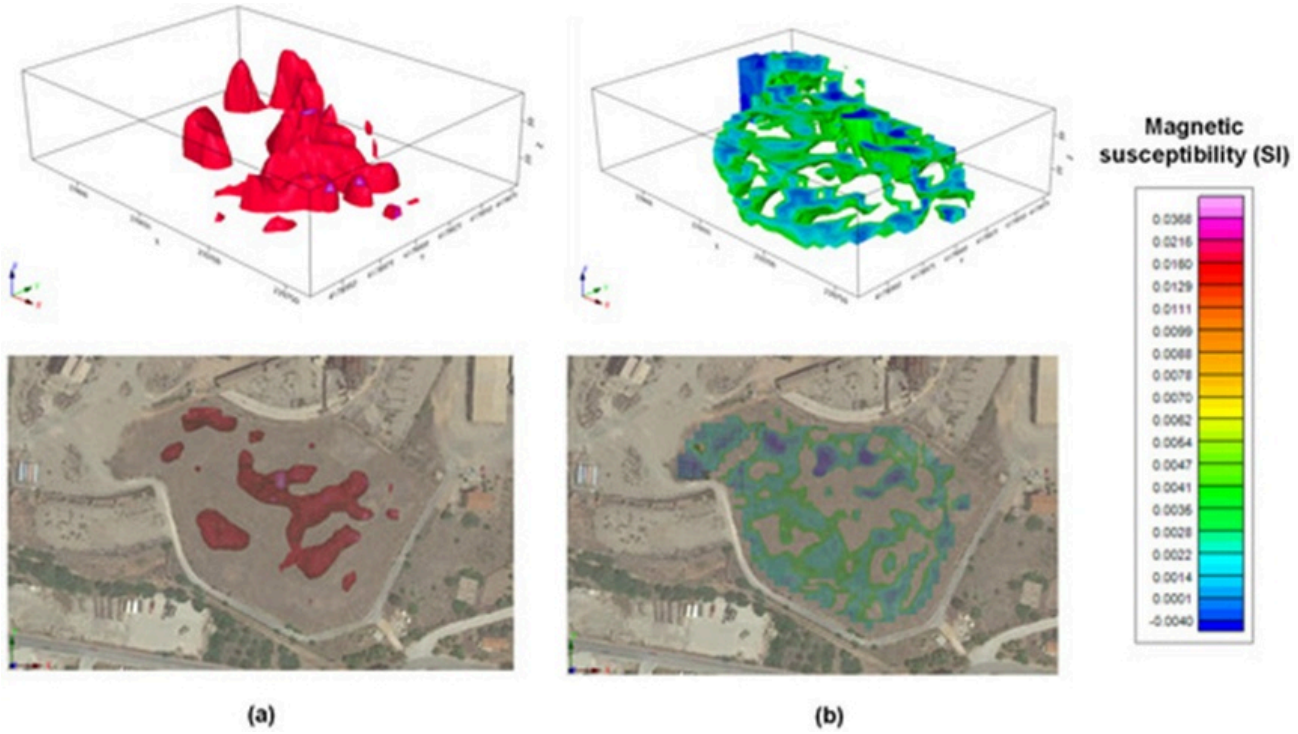

Figure 21. 3D model of magnetic susceptibility: (a) High magnetic susceptibility values; (b) Close to zero or negative magnetic susceptibility values.

© 2022 The Author(s). | Published by Agro Intelligence Research Press

Conclusion

The helicopter-borne magnetometry investigation conducted across the Lavrion repository has yielded new insights into the site's subsurface geology and the dispersal of its contained materials.

Collecting magnetic field readings via the CERBERUS UAV proved to be an exceptionally practical and streamlined approach, provided the endeavour is supported by a competent team with expertise spanning both geospatial technologies and geophysics. This survey mode permits the coverage of extensive land parcels within abbreviated operational windows, while additionally granting access to locations that would be effectively out of reach for ground crews—whether due to precipitous relief, impenetrable vegetative cover, or the threat posed by environmental contamination, as typified by hazardous waste sites or toxic repositories.

Scrutiny of the total magnetic intensity grid and its pole-reduced equivalent revealed striking inhomogeneity among the repository fill materials, confirming the presence of distinct compositional zones. In a complementary vein, the employment of the TILT derivative, built upon the findings of the Magnetic Field Reduction to the Pole (MFRP) operation, proves adept at throwing into sharp relief the linear interfaces that separate volumes of contrasting magnetic character. This transformation exposed a wealth of linear boundaries, testifying to a diversity of material types discriminated by their magnetic susceptibilities. Beyond this, the execution of the pseudo-gravity conversion allowed the zones hosting the repository's densest material packages to be singled out.

The assembly of a 3D model rooted in magnetic susceptibility data lent additional resolving power to the geophysical characterization effort, offering an all-encompassing view of the repository's structural anatomy. Most notably, sectors with high susceptibility amplitudes were traced to elevated concentrations of ferromagnetic agents such as iron and nickel, while domains of low or negative susceptibility aligned with materials deficient in ferromagnetic content yet enriched in diamagnetic elements—lead, arsenic, cadmium, and zinc serving as prominent examples. The ambient magnetic susceptibility background of the repository essentially mirrors the signature of the geological units disposed there. The introduction of specific chemical species perturbs this baseline, either elevating or depressing it, underscoring the principle that the ensuing interpretation must be conceived in relative, context-dependent terms rather than in absolute ones.

Viewed in its entirety, the aerial magnetometry programme completed at the Lavrion repository has generated a wealth of spatially explicit information regarding material distribution and composition, secured entirely through a non-invasive pathway. This outcome underscores the potency of UAV-deployed magnetometry as a geophysical reconnaissance tool.

These extended conclusions reaffirm the position of airborne magnetometry as an agile, high-impact methodology within geophysical surveying, establishing a robust foundation for subsequent exploratory ventures and research across both readily traversable and physically demanding environments.

Acknowledgements

None

Conflict of interest

The authors declare no conflicts of interest. The funders had no role in the design of the study, the collection, analysis, or interpretation of data, the writing of the manuscript, or the decision to publish the results. Additionally, the authors, Dimitris Perikleous, Katerina Margariti, and Pantelis Velanas, were employed by ACCELIGENCE Ltd. The remaining authors declare that the research was conducted in the absence of any commercial or financial relationships that could be construed as a potential conflict of interest.

© 2022 The Author(s). | Published by Agro Intelligence Research Press

Financial support

This research was funded by the European Union's Horizon Europe research and innovation program (Grant Agreement No. 101091885).

Ethics statement

None

Received: 18 Oct 2021 Revised: 22 Dec 2021 Accepted: 07 Jan 2022
Published online: 25 May 2022

Rights and permissions

Open Access The author(s) retain copyright. This article is licensed under the Creative Commons Attribution-NonCommercial-ShareAlike 4.0 International License. It may be shared and adapted for non-commercial purposes with appropriate attribution, an indication of changes, and distribution of adaptations under the same license. Third-party material may be subject to separate terms identified in its credit line. View the license at https://creativecommons.org/licenses/by-nc-sa/4.0/.

References

1. Sánchez F, Hartlieb P. Innovation in the mining industry: Technological trends and a case study of the challenges of disruptive innovation. Min Metall Explor. 2020;37:1385-99.

2. Levin LA, Amon DJ, Lily H. Challenges to the sustainability of deep-seabed mining. Nat Sustain. 2020;3:784-94.

3. Kariri E, Louati H, Louati A, Masmoudi F. Exploring the advancements and future research directions of artificial neural networks: A text mining approach. Appl Sci. 2023;13:3186.

4. Ediriweera A, Wiewiora A. Barriers and enablers of technology adoption in the mining industry. Resour Policy. 2021;73:102188.

5. Park S, Choi Y. Applications of unmanned aerial vehicles in mining from exploration to reclamation: A review. Minerals. 2020;10:663.

6. Fernández-Hernandez J, González-Aguilera D, Rodríguez-Gonzálvez P, Mancera-Taboada J. Image-based modelling from unmanned aerial vehicle (UAV) photogrammetry: An effective, low-cost tool for archaeological applications. Archaeometry. 2014;57:128-45.

7. Chandra M, Tanzi TJ. Drone-borne GPR design: Propagation issues. C R Phys. 2018;19:72-84.

8. Saponaro A, Dipierro G, Cannella E, Panarese A, Galiano AM, Massaro A. A UAV-GPR fusion approach for the characterization of a quarry excavation area in Falconara Albanese, Southern Italy. Drones. 2021;5:40.

9. Babu GA, Krishna GV, Tiwari VM, Antony R, Suraj CS, Vikas KT, et al. Drone-borne magnetic measurements in India. Curr Sci. 2020;119:598-600.

10. Accomando F, Vitale A, Bonfante A, Buonanno M, Florio G. Performance of two different flight configurations for drone-borne magnetic data. Sensors. 2021;21:5736.

© 2022 The Author(s). | Published by Agro Intelligence Research Press

11. Walter CA, Braun A, Fotopoulos G. Impact of three-dimensional attitude variations of an unmanned aerial vehicle magnetometry system on magnetic data quality. Geophys Prospect. 2018;67:465-79.

12. Walter C, Braun A, Fotopoulos G. Characterizing electromagnetic interference signals for unmanned aerial vehicle geophysical surveys. Geophysics. 2021;86:J21-32.

13. Mandlburger G, Pfennigbauer M, Wieser M, Riegl U, Pfeifer N. Evaluation of a novel UAV-borne topo-bathymetric laser profiler. Int Arch Photogramm Remote Sens Spat Inf Sci. 2016;XLI-B1:933-9.

14. Porras D, Carrasco J, Carrasco P, Alfageme S, Gonzalez-Aguilera D, Lopez Guijarro R. Drone magnetometry in mining research. An application in the study of Triassic Cu-Co-Ni mineralizations in the Estancias Mountain Range, Almería (Spain). Drones. 2021;5:151.

15. Walter C, Braun A, Fotopoulos G. High-resolution unmanned aerial vehicle aeromagnetic surveys for mineral exploration targets. Geophys Prospect. 2019;68:334-49.

16. Cunningham M, Samson C, Wood A, Cook I. Aeromagnetic surveying with a rotary-wing unmanned aircraft system: A case study from a zinc deposit in Nash Creek, New Brunswick, Canada. Pure Appl Geophys. 2018;175:3145-58.

17. Parvar K, Braun A, Layton-Matthews D, Burns M. UAV magnetometry for chromite exploration in the Samail ophiolite sequence, Oman. J Unmanned Veh Syst. 2017;6:57-69.

18. Accomando F, Bonfante A, Buonanno M, Natale J, Vitale S, Florio G. The drone-borne magnetic survey as the optimal strategy for high-resolution investigations in presence of extremely rough terrains: The case study of the Taverna San Felice quarry dike. J Appl Geophys. 2023;217:105186.

19. García JC, García PC, Sanchiz DP, Nieto IM, Blázquez CS, Hurtado PH. Drone magnetic and time domain electromagnetic exploration in metamorphic formations: Tool for the identification of strategic sites for aquifer exploitation. Appl Sci. 2023;13:10949.

20. Antoniadis V, Thalassinos G, Levizou E, Wang J, Wang SL, Shaheen SM, et al. Hazardous enrichment of toxic elements in soils and olives in the urban zone of Lavrio, Greece, a legacy, millennia-old silver/lead mining area and related health risk assessment. J Hazard Mater. 2022;434:128906.

21. Voudouris P, Melfos V, Melfou M, Tarantola A, Frenzel M, Spry PG, et al. Molybdenite Re-Os geochronology and conditions of formation of potassic and sodic-calcic alteration associated with the Plaka Porphyry Mo-Cu system, Lavrion, Greece. J Geochem Explor. 2024;270:107609.

22. Voudouris P, Melfos V, Mavrogonatos C, Photiades A, Moraiti E, Rieck B, et al. The Lavrion Mines: A unique site of geological and mineralogical heritage. Minerals. 2021;11:76.

23. Frenzel M, Voudouris P, Cook NJ, Ciobanu CL, Gilbert S, Wade BP. Evolution of a hydrothermal ore-forming system recorded by sulfide mineral chemistry: A case study from the Plaka PB-Zn-Ag deposit, Lavrion, Greece. Miner Depos. 2021;57:417-38.

24. Voudouris P, Melfos V. The Lavrion mines: Geological, metallogenic and mineralogical overview. ResearchGate. 2023;36-53.

25. Bonsall TA, Spry PG, Voudouris PC, Tombros S, Seymour KS, Melfos V. The geochemistry of carbonate-replacement Pb-Zn-Ag mineralization in the Lavrion District, Attica, Greece: Fluid inclusion, stable isotope, and rare earth element studies. Econ Geol. 2011;106:619-51.

26. Lavreotiki UNESCO Global Geopark. UNESCO. https://www.unesco.org/en/iggp/geoparks/lavreotiki (accessed on 25 September 2024).

© 2022 The Author(s). | Published by Agro Intelligence Research Press

27. Perikleous D, Koustas G, Velanas S, Margariti K, Velanas P, Gonzalez-Aguilera D. A novel drone design based on a reconfigurable unmanned aerial vehicle for wildfire management. Drones. 2024;8:203.

28. Open Category—Low Risk—Civil Drones. EASA. 2024. https://www.easa.europa.eu/en/domains/drones-air-mobility/operating-drone/open-category-low-risk-civil-drones (accessed on 25 September 2024).

29. Aleksandrov D, Penkov I. Optimization of lift force of mini quad-rotor helicopter by changing of gap size between rotors. Solid State Phenom. 2013;198:226-31.

30. Cao W, Qing H, Xu X, Liu C, Chen S, Zhong Y, et al. Pre-archaeological investigation by integrating unmanned aerial vehicle aeromagnetic surveys and soil analyses. Drones. 2022;6:243.

31. Malehmir A, Dynesius L, Paulusson K, Paulusson A, Johansson H, Bastani M, et al. The potential of rotary-wing UAV-based magnetic surveys for mineral exploration: A case study from Central Sweden. Lead Edge. 2017;36:552-7.

32. Shahsavani H. An aeromagnetic survey carried out using a rotary-wing UAV equipped with a low-cost magneto-inductive sensor. Int J Remote Sens. 2021;42:8805-18.

33. Kim B, Jeong S, Bang E, Shin S, Cho S. Investigation of iron ore mineral distribution using aero-magnetic exploration techniques: Case study at Pocheon, Korea. Minerals. 2021;11:665.

34. Utsugi M. 3-D inversion of magnetic data based on the L1-L2 norm regularization. Earth Planets Space. 2019;71:73.

35. Yaoguo L, Douglas W, Oldenburg. Fast inversion of large-scale magnetic data using wavelet transforms and a logarithmic barrier method. Geophys J Int. 2003;152:251-65.

36. Reynolds JM. An introduction to applied and environmental geophysics. Chichester, UK: John Wiley and Sons Ltd. 2011. p. 796.

37. Zheng Y, Li S, Xing K, Zhang X. Unmanned aerial vehicles for magnetic surveys: A review on platform selection and interference suppression. Drones. 2021;5:93.

38. Hrvoic I, Hollyer G, Wilson M, Szeto A. Development of a new high sensitivity potassium magnetometer for near surface geophysical mapping. In: Proceedings of the Symposium on the Application of Geophysics to Engineering and Environmental Problems; San Antonio, TX, USA; 2003.

© 2022 The Author(s). | Published by Agro Intelligence Research Press